Earth and Planetary Science Letters 605 (2023) 118035

Contents lists available at ScienceDirect

Earth and Planetary Science Letters

journal homepage: www.elsevier.com/locate/epsl

An astronomical timescale for the Permian-Triassic mass extinction reveals a two-step, million-year-long terrestrial crisis in South China

Fanghui Hua [a], Longyi Shao [a,*], Tianchang Zhang [a], David P.G. Bond [b,*], Xuetian Wang [a], Juan Wang [c], Zhiming Yan [d], Jing Lu [a], Jason Hilton [e]

[a] State Key Laboratory of Coal Resources and Safe Mining and College of Geoscience and Surveying Engineering, China University of Mining and Technology (Beijing), Beijing 100083, China
[b] School of Environmental Sciences, University of Hull, HU6 7RX, UK
[c] School of Resources and Environment, Henan Polytechnic University, Jiaozuo 454003, Henan Province, China
[d] Institute of Architectural Engineering, Weifang University, Weifang 261061, Shandong Province, China
[e] School of Geography, Earth and Environmental Sciences, University of Birmingham, B15 2TT, UK

ARTICLE INFO

Article history:
Received 22 September 2022
Received in revised form 26 January 2023
Accepted 28 January 2023
Available online xxxx
Editor: A. Jacobson

Keywords:
Permian-Triassic
astrochronology
carbon isotopes
mass extinction
terrestrial plants
South China

ABSTRACT

The Permian-Triassic Mass Extinction (PTME) is the greatest biotic crisis of the Phanerozoic. In terrestrial settings, the PTME appears to have been diachronous and it has been suggested that losses initiated before the marine crisis. We examine organic carbon-isotope ($\delta^{13}C_{org}$) and geochemical proxies for environmental change in a palaeotropical wetland succession from southwest China. A newly constructed astronomical timescale provides a temporal framework for constraining the timing of the terrestrial PTME. Two major, negative carbon isotope excursions (CIEs) of 5.3‰ and 3.9‰ are observed between the top of the (Permian) Xuanwei Formation and the middle of the (Permian-Triassic) Kayitou Formation respectively. Our cyclostratigraphic model suggests that carbon cycle destabilization lasted ~0.6 ± 0.1 Myr. We calculate total erosion rates for basaltic landscapes as a proxy for volumes of bare soil resulting from deforestation. Two phases of accelerated erosion saw denudation rates rise over a ~1 Myr period from ~150 t/km2/yr in the upper Xuanwei Formation (Permian) to >2000 t/km2/yr at the base of the Dongchuan Formation (Triassic). Calibrating the collapse of terrestrial ecosystems indicates that although the equatorial terrestrial PTME initiated before the marine crisis, it was a protracted process with the final coup-de-grâce not until ~ 700 ky later. This has a bearing on extinction scenarios in which the terrestrial PTME is a causal factor in marine losses via enhanced nutrient runoff, because the final devastation on land post-dates the much more abrupt marine PTME.

1. Introduction

The Permian-Triassic Mass Extinction (PTME) is the most catastrophic loss of life in Earth history with > 90% marine and > 70% terrestrial species lost (Erwin, 2015). Carbon isotope studies combined with radio-isotopic dating of marine strata constrained the duration of the marine crisis to just 61 ± 48 kyr, or 31 ± 31 kyr (Burgess et al., 2014; S.Z. Shen et al., 2019). In contrast, the full duration of the terrestrial PTME is still not well understood in different parts of the world (Shen et al., 2011; Zhang et al., 2016; Fielding et al., 2019) and the placement of the terrestrial Permian-Triassic boundary (PTB) has been problematic in some locations (Bercovici et al., 2015; Zhang et al., 2016; Chu et al., 2020; Wignall et al., 2020). High-precision radioisotope dating, and high-resolution biostratigraphy and chemostratigraphy show that the terrestrial and marine extinctions were not isochronous, with an earlier onset on land (Fielding et al., 2019; Chu et al., 2020; Lu et al., 2022). Some studies have suggested that floral extinctions were gradual (Xiong and Wang, 2016), prior to a final catastrophic extinction (Xu et al., 2022). Geochemical proxies from marine strata suggest there were two phases of vegetation collapse (Aftabuzzaman et al., 2021) with two corresponding pulses of increased terrestrial input (Huang et al., 2022) between the latest Permian and earliest Triassic. This implies that the terrestrial PTME was not a single, instantaneous event that predated (and potentially drove) the marine crisis (Fielding et al., 2019; Lu et al., 2022) but had a more complex history. The pattern of terrestrial extinctions appears to vary from one region to the next, potentially linked to

* Corresponding authors.
E-mail addresses: ShaoL@cumtb.edu.cn (L. Shao), D.Bond@hull.ac.uk (D.P.G. Bond).

https://doi.org/10.1016/j.epsl.2023.118035

differences in latitude, biodiversity and ecological stress (Feng et al., 2020).

In southwestern (SW) China, carbon isotopes and radio-isotopic dating have not delivered consensus on the stratigraphic position of the terrestrial PTME and the PTB (Shen et al., 2011; Chu et al., 2020; Wu, 2020). The PTB has been placed at the Kayitou / Dongchuan formational contact (Zhang et al., 2016, 2021) but a major negative carbon isotope excursion (CIE; similar to that recorded in latest Permian marine strata) that initiates at the top of the Xuanwei Formation undermines this placement (Chu et al., 2020). Plant fossils indicate the regional collapse of *Gigantopteris* rainforests and the cessation of peat formation at the base of the Kayitou Formation (Yu et al., 2015; Shao et al., 2020; Xu et al., 2022). However, palynology indicates a moderately rich Palaeozoic flora persisted after the uppermost coal at the top of the Xuanwei Formation, leading to suggestions that there was no terrestrial extinction (Xiong and Wang, 2016) or that losses were relatively muted when compared to those indicated by the plant macrofossil record (Xu et al., 2022). Recently obtained volcanic ash zircon U–Pb age data from several terrestrial sections in South China support the placement of the PTB in the basal part of the Kayitou Formation (Wu, 2020). However, due to sedimentary facies variations in terrestrial strata and the laterally discontinuous distribution of volcanic ashes across the region, some have questioned this stratigraphic framework (e.g., Zhang et al., 2021). Notwithstanding issues surrounding the placement of the PTB, a dramatic disruption of terrestrial ecosystems is recognized at the base of the Kayitou Formation across the region.

Basaltic weathering is sensitive to climate (Chen et al., 2020) and has been invoked as a driver of Permian-Triassic climate change (Yang et al., 2022). During the Permian-Triassic interval, the South China block lay near the equator (Huang et al., 2018) where a humid climate experienced rapid warming (Yang et al., 2022). Sediments were sourced from the basaltic Emeishan Large Igneous Province (LIP) and the Kangdian Oldland to the west (Wang et al., 2020). SW China thus provides a valuable record of basaltic weathering during the PTME. Our basaltic weathering and carbon isotope records are set within a temporal framework derived from Milankovitch periodicity signals in borehole gamma ray (GR) data combined with high-precision zircon dating of ash layers (e.g. Wang et al., 2018; Li et al., 2019; Wu, 2020). This astronomical timescale is used to constrain the timing and duration of the terrestrial PTME, with implications for scenarios in which the terrestrial crisis drove marine losses.

2. Geological setting

We examined a Late Permian-Early Triassic borehole core drilled 30 km northeast of Xuanwei City, Yunnan (26° 25' 32.846" N; 104° 15' 10.565" E) on the SW margin of the Yangtze craton (Fig. 1A), plus two further cores drilled nearby (see Methods for details). Terrestrial Permian-Triassic strata include, from oldest to youngest, the Emeishan Basalt Formation overlain unconformably by the sedimentary Xuanwei, Kayitou and Dongchuan formations, each of which lies conformably over that below. The sedimentary source was the Kangdian Oldland which was uplifted through this interval by the Emeishan mantle plume (Fig. 1B) (Zhang et al., 2016; Wang et al., 2020).

The Xuanwei Formation - the youngest Permian coal-bearing strata - consists of gray-black to light gray mudrocks, sandstones and coals that formed in an alluvial plain setting (Wang et al., 2020). Late Permian peat-forming plant ecosystems, dominated by the gigantopterids *Gigantopteris* and *Gigantonoclea*, are widely distributed in South China (Fig. 1C). These plants, together with *Lobatannularia*, *Paracalamites* and *Pecopteris* form the Cathaysia palaeoflora (Yu et al., 2015) that flourished in a warm, humid tropical climate. Correlation of stratigraphic records from different sections in South China shows that abundant volcanic ash occurs around the contact between the Xuanwei and Kayitou formations (He et al., 2014). The ash layers were initially thought to represent regional eruptive activity associated with a volcanic arc along the margin of the South China Block (He et al., 2014), but have also been linked to the Siberian Traps LIP due to their temporal coincidence (Shen et al., 2011; Burgess et al., 2014). The overlying Kayitou Formation consists of grayish-green fine-grained clastic rocks, deposited in shallow, coastal terrestrial lagoon environments (Bercovici et al., 2015). Plants from the Kayitou Formation are sparse and coals are absent. Sporadic, non-reworked *Gigantopteris* remains are known from the bottom of the Kayitou Formation, alongside abundant remains of the spinicaudatans *Euestheria* and *Palaeolimnadia* and the Triassic plants *Annalepis*/*Lepacylotes* (Fig. 1c) (Feng et al., 2020; Xu et al., 2022). The overlying Dongchuan Formation comprises red, fine-grained clastic rocks deposited in a braided river setting (Bercovici et al., 2015) in an arid climate (Fig. 1C). It is unclear if the lack of plants in the Dongchuan Formation is a function of an unsuitable depositional environment, or the non-preservation of organic matter in oxidizing settings (Xu et al., 2022). However, adpressions of plant fossils are commonly found in red beds, so the absence of these in the Dongchuan Formation may well be a function of a lack of flora in the environment at the time of deposition (see e.g. Trümper et al., 2020).

3. Methods

We analyzed 39 samples from the Hanjiagou 401 (H401) core (26° 25' 32.846" N; 104° 15' 10.565" E) for organic carbon isotopes ($\delta^{13}C_{org}$), total organic carbon (TOC), and trace and major element concentrations 50 m either side of the Xuanwei / Kayitou formational contact. $\delta^{13}C_{org}$ was measured from decarbonated material using isotope ratio mass spectrometry (Thermo Finnigan MAT-253; absolute analysis error ±0.1‰). TOC was determined using a carbon sulfur analyzer (Eltra-CS-580A; absolute analysis error ±0.2%). Concentrations of trace elements were determined by High-Resolution Inductively Coupled Plasma Mass Spectrometer (ThermoFisher Element XR; relative analysis error ±5%). Hg was measured by mercury analyzer (Lumex RA-915; relative analysis error ±5%). Major elements were measured by X-ray fluorescence spectrometer (Panalytical PW2404). All analyses were performed at the Beijing Research Institute of Uranium Geology. The Chemical Index of Alteration (CIA) quantifies alteration of feldspars to clays in mudstones, and we employ this as a proxy for changes in climate-driven weathering. High CIA values indicate hot, humid climates (Fielding et al., 2019).

High-resolution borehole and outcrop logging data has been widely applied for the analysis of Milankovitch cycles and to estimate sedimentation rates and/or calibrate the ages of geological events (Huang et al., 2011; Hinnov, 2013; Li et al., 2019; Cui et al., 2021). In particular, Gamma Ray (GR) logging can be used to establish a robust timescale when integrated with other chronostratigraphic data in clastic shelf sediments (Xu et al., 2020). We analyzed gamma ray logs from three boreholes chosen for their similar lithostratigraphy and relative proximity (H401, Shuanghe 301 [S301], 28 km to the NE of H401 [26° 38' 20.258" N; 104° 24' 1.714" E] and Hanjiagou 601 [H601], ~1.4 km to the NE of H401 [26° 26' 7.86" N; 104° 15' 41.671" E]) using the software package *Acycle* (Li et al., 2019). We applied the multi-taper method (MTM) of spectral analysis within *Acycle* to evaluate astronomical frequencies in the detrended GR using the LOWESS method (including high-pass filtering, polynomial fitting, moving average, and local regression smoothing). In order to identify stratigraphic frequencies and tuned GR series, and to detect changing accumula-

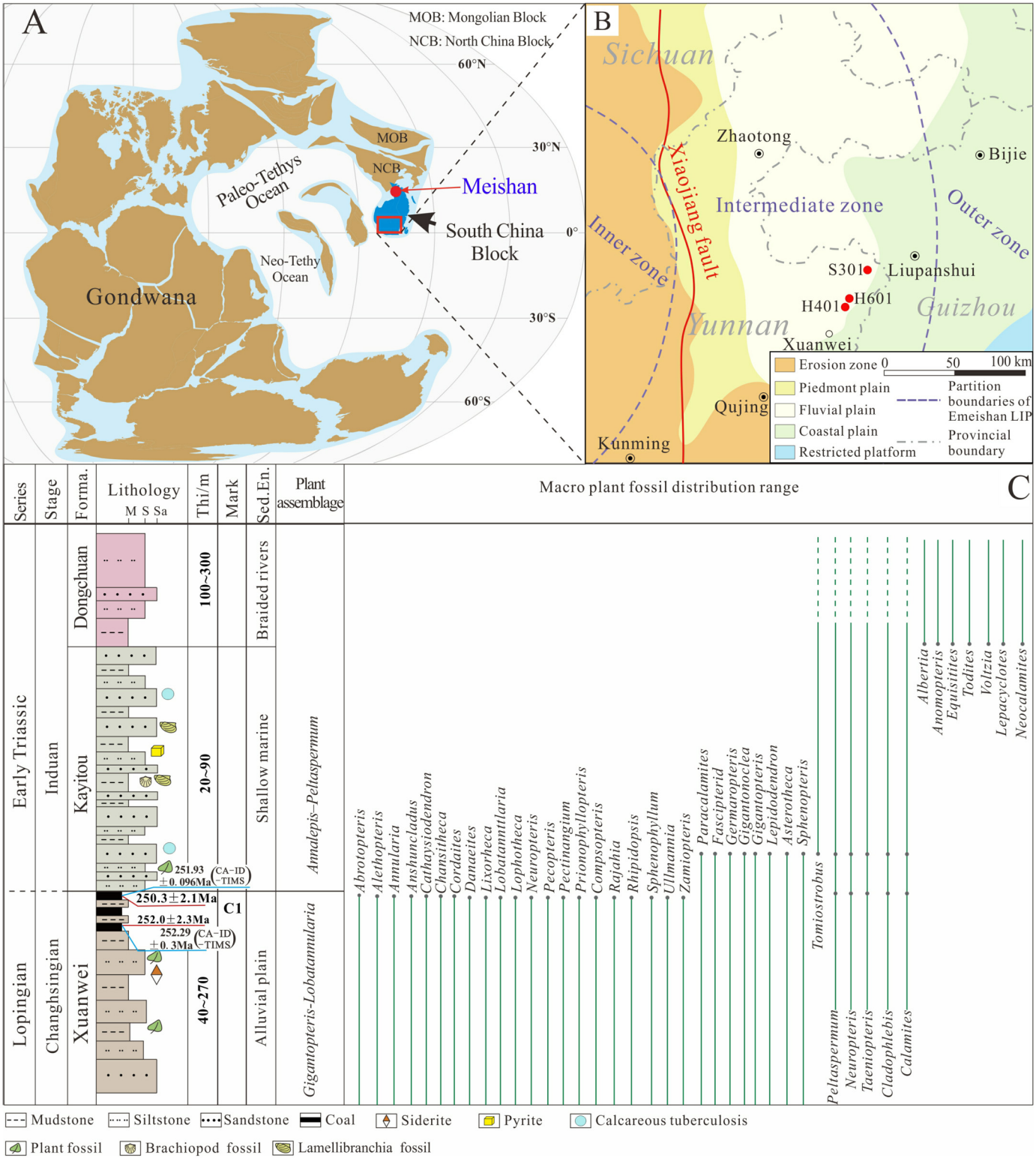

Fig. 1. Location and geological context for the studied locations. A) Late Permian paleogeography (adapted from Huang et al., 2018); B) Paleogeography of SW China (Shao et al., 2013) with borehole locations; C) Sedimentary log for the PTB transition at Xuanwei City, Yunnan. Lithology from Liu et al. (2020), macro plant fossil distribution range from Xu et al. (2022), environments from Shao et al. (2013) and Bercovici et al. (2015), and ages from Wang et al. (2018) and Wu (2020). Abbreviations: Forma. = Formation; M = mudstone; S = siltstone; Sa = sandstone; Thi/m = thickness in metres; Mark = marker beds; Sed. En. = sedimentary environment.

tion rates, a sliding-window spectral analysis was performed using evolutive Fast Fourier transform (FFT) spectrograms. We used the "Age scale" toolbox in *Acyle* to establish an astronomically tuned timescale (Li et al., 2019). The "Correlation Coefficient" toolbox was used for astronomical inspection and to estimate sedimentation rates. This approach employs the correlation coefficient between the power spectra of a proxy series and that of an associated astronomical forcing series, converting the proxy series to time for a range of "test" sedimentation rates (Li et al., 2018). The number of astronomical parameters contributing to the estimated sedimenta-

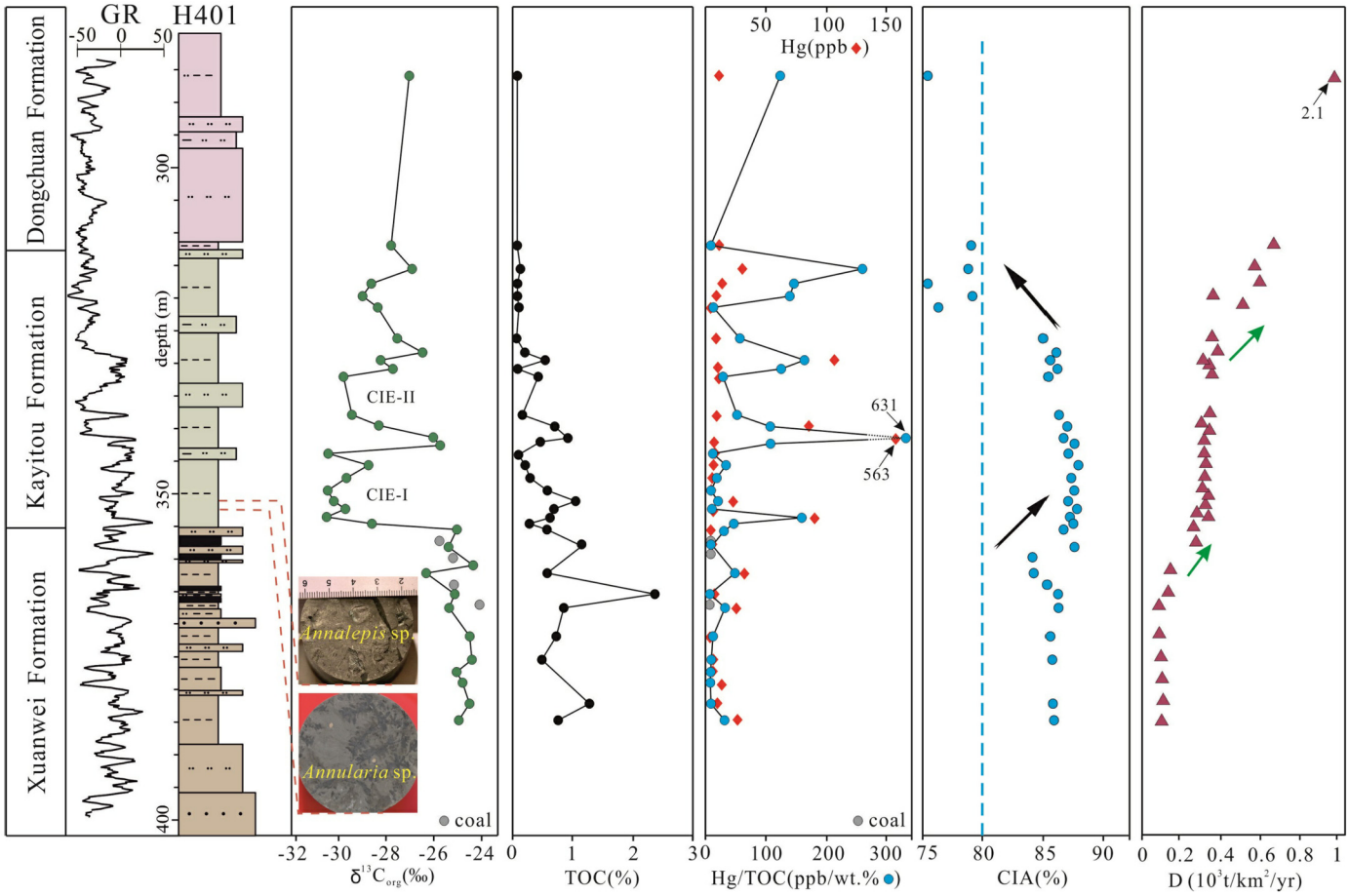

Fig. 2. Organic carbon isotopes ($\delta^{13}C_{org}$), total organic carbon (TOC), Hg, Hg/TOC, Chemical Index of Alteration (CIA) and derived denudation rate (D) in the H401 core. The denudation rate shown here was calculated based on the equivalent charge ratio of the divisions relative to the average basic source rock (see also Figure S2).

tion rates is taken into account. The null hypothesis of no astronomical forcing is tested using a Monte Carlo simulation approach (Li et al., 2018).

4. Results

4.1. Geochemistry

$\delta^{13}C_{org}$ values in the Xuanwei Formation are relatively heavy and stable, varying from -24‰ to -25.9‰ (mean ($\bar{x}$) = -24.9‰). $\delta^{13}C_{org}$ values from the Kayitou Formation vary from -25.1‰ to -30.4‰ ($\bar{x}$ = -26.1‰) and include two negative excursions. The earlier of these excursions, in the lowest part of the Kayitou Formation, sees a negative shift of 5.3‰ (CIE-1) and is the largest of the two shifts. CIE-1 appears to have been protracted, extending through approximately 10 m of the sedimentary succession (Fig. 2). These strata record a change to gray green coloration and their flora is of low diversity, comprising fragmentary, small lycopods (*Annalepis*). Following CIE-1, δ13Corg values return to the background levels seen in the Xuanwei Formation, before a second negative excursion occurs in the middle of the Kayitou Formation (a shift of 3.9‰, CIE-2).

TOC concentrations in the Xuanwei Formation range from 0.56% to 3.08% ($\bar{x}$ = 1.25%). TOC concentrations decrease significantly in the lower and middle part of the Kayitou Formation, and are highly variable, with some samples having values < 0.3% while others have > 1% TOC. TOC values in the upper part of the Kayitou and overlying Dongchuan Formation are extremely low, typically < 0.1%. Overall, the trend of TOC reduction and the $\delta^{13}C_{org}$ negative excursions are synchronous (Fig. 2).

Hg concentrations in the Xuanwei Formation range from 1.02–33.6 ppb ($\bar{x}$ 12.42 ppb; Table S1). The Kayitou Formation has three distinct Hg peaks (Fig. 2). The first, of 86.2 ppb, occurs with CIE-1 at the base of the Formation. The second, of 563.4 ppb, is 15 m higher, while the third, of 109.4 ppb, is 10 m higher still. The Dongchuan Formation sees Hg fall to baseline (i.e. mean) values typical of the Xuanwei Formation. Peak Hg values fall within the typical range for the PTB (134–641 ppb; Grasby et al., 2019). These Hg peaks withstand normalization to TOC (to account for Hg binding to organic matter; J. Shen et al., 2019) and to Al (to account for terrestrial input; Fig. S1). A fourth Hg/TOC peak near the top of the Kayitou Formation is an artefact of very low TOC (0.12%) (Fig. 2).

The concentrations of oxides of major elements, which are used here to infer erosion of the basaltic landscape, are provided in full in Supplementary Table 1. All samples have variable concentrations of SiO_2 (27.0-54.1%), Al_2O_3 (7.0-26.2%), Fe_2O_3 (2.6-25.4%), CaO (0.51-2.86%), K_2O (0.1-4.2%) and Na_2O (0.03-4.17%). TiO_2 concentrations (mostly > 5.0%) are well above average values for upper continental crust (0.5%; Taylor et al., 1981), while they closely resemble the high-Ti basalt (average of 4.23%) from the Emeishan LIP (Xiao et al., 2004). Throughout our studied strata, Al_2O_3, CaO, Na_2O and K_2O do not show any significant variations in their concentrations (Table S1). Concentrations of FeO are significantly higher in the Kayitou Formation than in the Xuanwei Formation. Full results of the trace element analyses are provided in Supplementary Tables 2 and 3. In summary, trace elements include Nb contents of 23.0-88.0 μg/g, Y contents of 20.0-82.4 μg/g, Zr contents of 153.2-600.3 μg/g and REE contents of 150.4-799.4 μg/g.

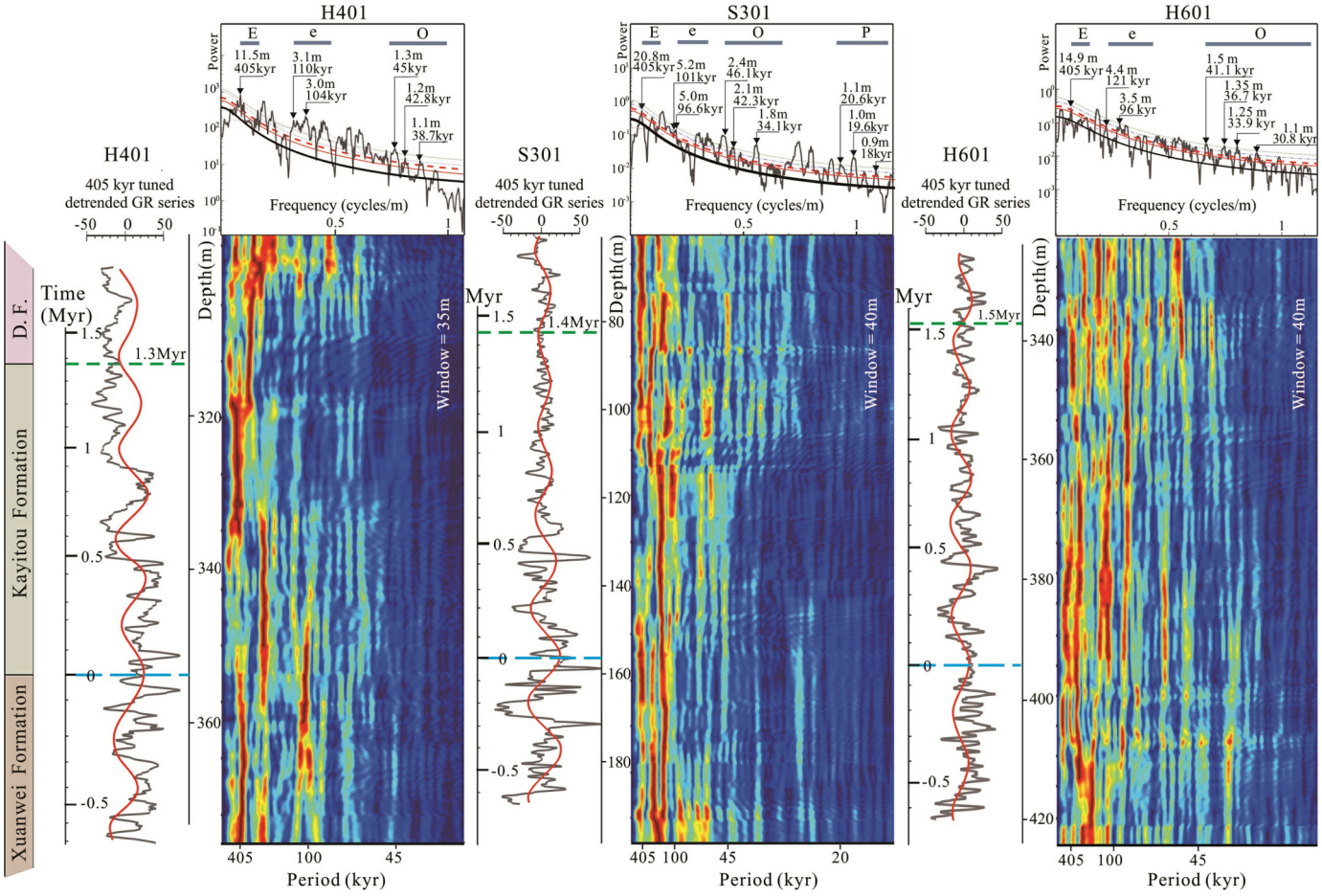

Fig. 3. Interpreted cyclostratigraphy of the H401, S301 and H601 borehole cores in the depth (meters) domain and tuning to the time domain. GR data are shown with their evolutive FFT spectra using 35 m (H401) and 40 m (S301 and H601) sliding windows and filtered cycles. The green, blue and red dashed curves represent confidence levels of 99%, 95%, and 90%, respectively. The labels E, e, O, and P represent the 405-kyr long eccentricity, 100-kyr eccentricity, obliquity, and precession cycles, respectively. Abbreviation: D.F. = Dongchuan Formation.

The Chemical Index of Alteration (CIA) reflects the extent of alteration of feldspars to clays in mudstones and is a proxy for changes in weathering conditions controlled by paleoclimate. Higher CIA values indicate more humid and hot climates (Fielding et al., 2019). The A-CN-K diagram tests the reliability of CIA values in this study and picks out deviations from the idealized weathering trend (Fig. S1). The CIA values were calibrated by the method: $CIA_{corr} = [Al_2O_3/(Al_2O_3+CaO^*+Na_2O+K_2O_{corr})] \times 100$ (Fedo et al., 1995; Panahi et al., 2000; Xu and Shao, 2018) and are shown in Fig. 2. CIA values from the Xuanwei Formation and the lower part of the Kayitou Formation are relatively stable and average 86.3%, though there is a fall to approximately 83% near the top of the Xuanwei Formation. Near the top of the Kayitou Formation CIA values decrease significantly to approximately 80% and these low values extend into the overlying Dongchuan Formation (79.5%) (Fig. 2).

4.2. Constraining the timeframe of the Kayitou formation

Previous studies of the Late Permian-Early Triassic stratigraphy in South China have identified 405 kyr eccentricity, 125–95 kyr eccentricity, 30–45 kyr obliquity, and 17–20 kyr equinox astronomical cycles (Wu et al., 2013; Li et al., 2016; Wang et al., 2020). These studies employed spectral analysis with high-precision zircon dates as constraints. Our results are consistent with these previous studies and the above have been used as orbital parameter periods for our cyclostratigraphic analysis.

MTM power spectra analysis of the detrended GR series of the three boreholes in our study reveal some prominent astronomical cycles (Fig. 3 A). In borehole H401, stratigraphic cycles identified with cycle thicknesses of 11.5 m, 5.3 m, 4.5 m, 3.1 m, 3.0 m, 2.5 m, 2.2 m, 1.9 m, 1.7 m, 1.6 m, 1.5 m and 1.3 m are above the 99% confidence level, and those of 2.3 m, 1.2 m and 1.1 m are above the 95% confidence level. The evolutive FFT of the H401 borehole core shows that the GR series is characterized by cyclic variations of 11.5 m, 5.6 m, 3 m, 1.7 m and 1.3 m in the interval between 332 m and 378 m in the succession, and that a stable 11.5 m cycle is recorded by the overlying strata (Fig. 3). In borehole S301, stratigraphic cycles identified with cycle thicknesses of 7.0 m, 5.2 m, 5.0 m, 3.3 m, 2.9 m, 2.4 m, 2.1 m, 1.8 m, 1.3 m, 1.2 m, 1.1 m, 1.0 m and 0.9 m are above the 99% confidence level, and those of 20.8 m and 10.5 m are above the 95% confidence level. The evolutive FFT of the S301 core shows that the GR series is characterized by cyclic variations of 20.8 m, 10.5 m, 7 m and 5 m in the interval between 71 m and 196 m in the succession (Fig. 3). In borehole H601, stratigraphic cycles identified with cycle thicknesses of 5.5 m, 3.5 m, 3.1 m, 2.2 m, 1.8 m, 1.5 m, 1.35 m, 1.25 m, 1.1 m and 1 m are above the 99% confidence level, and those of 14.9 m 4.4 m and 2.6 m are above the 95% confidence level (Fig. 3). The evolutive FFT of H601 shows that the GR series is characterized by cyclic variations of 14.9 m, 5.5 m, 4.4 m, 3.5 m, 2.2 m, 1.8 m, 1.5 m, 1.35 m, 1.25 m, and 1 m in the interval between 330 m and 420 m in the succession (Fig. 3).

The correlation coefficient (COCO) analysis in *Acycle* is a tool for evaluating the optimal sedimentation rates and the effects of astronomical forcing throughout the Phanerozoic. The COCO results suggest that the optimal sedimentation rates of the targeted interval are 2.9 cm/kyr in H401, 5.5 cm/kyr in S301 and 3.5 cm/kyr in H601, respectively (Fig. S3). The H_0 significance level of non-astronomically driven cycles corresponding to the optimum sedimentation rate in each borehole section is lower than 0.1%, indicating that sedimentation was significantly affected by astronomical forcing. Multiplying the optimal sedimentation rates with 405 kyr orbital parameter periods implies that the cycles at 11.5 m in the H401 record, 20.8 m in S301, and 14.9 m in H601 represent 405 kyr eccentricity. The 405-kyr-tuned MTM power spectra have peaks at 405, 188, 158, 110, 104, 78, 62, 57, 45, 42 and 38 kyr periods in H401 (Fig S4a), peaks at 405, 137, 101, 96, 46, 42, 34, 26, 24, 20, 19 and 18 kyr periods in S301 (Fig S4b), and peaks at 405, 151, 121, 96, 57, 51, 49, 41.1, 36.7, 33.9 and 30.8 kyr periods in H601 (Fig S4c). The astronomical solution of Berger89 or Laskar04 suggests that the 405 kyr periods represent the long eccentricity cycle, the 95 kyr to 125 kyr periods represent the eccentricity cycle, the 30 kyr to 45 kyr periods represent the obliquity cycle, and the 17 kyr to 21 kyr periods represent the precession cycle. The remaining peaks might be a function of sedimentation processes themselves, or could be related to other astronomical drivers (see Ma et al., 2017; Huang et al., 2021). The precession signal is unstable in geological record and is easily lost, and as such this signal has gone unidentified in numerous other studies (e.g., Huang et al., 2011; Li et al., 2016; Wang et al., 2020; Huang et al., 2021). In this study, we have identified the precession signal only in the S301 borehole succession, where it can be used to lend confidence to the results and the interpretation of the 405 kyr signals. It is therefore reasonable to suggest that the 405 kyr eccentricity periods are recorded in all three borehole successions. The interpreted periods and timeframes are consistent with orbital periods recognized in other sections in South China by Huang et al. (2011) and Li et al. (2016). The evolutive FFT show the 405 kyr periods and 95 kyr to 125 kyr periods have stable signals within the target interval of each borehole record. These vertical stable passbands provide strong evidence for astronomical forcing. As the 405 kyr period is considered to be largely stable throughout geological history (Hinnov, 2013), we adopt 405 kyr-tuning in order to build a floating astronomical timescale. We did this for each individual borehole in order to obtain a consistent period for the three different successions. Although the timescales for each borehole are different, the 405 kyr cycle corresponds to the correct period for the targeted interval. The 100 kyr-tuning results show an uncertainty of about one 100 kyr cycle within the 405 kyr cycle in the target interval (Fig. 5). This can be attributed to uncertainties in the astronomical solution and variations in sedimentation rates within the 405 kyr cycle (Li et al., 2016). The resulting estimated durations for the Kayitou Formation are 1.3 $\pm$ 0.1 Myr, 1.4 $\pm$ 0.1 Myr and 1.5 $\pm$ 0.1 Myr based on the H401, S301 and H601 records respectively (Fig. 3). That these estimates are similar suggests that our results are reliable. The slight discrepancies in the estimates of time recorded by the Kayitou Formation in the three different locations are possibly a function of the gradational transition between the Kayitou and Dongchuan Formations and uncertainty regarding the precise placement of the formational boundary.

5. Discussion

5.1. Massive erosion of basaltic landscapes across the Permo-Triassic boundary

Sedimentological evidence shows that Late Permian clastic sediments in southwestern China were mainly sourced from Kangdian Oldland which was continuously uplifted by the Emeishan mantle plume (Wang et al., 2020). The ratios of Al_2O_3/TiO_2, Zr/TiO_2, and Nb/Y as well as REE distribution patterns are stable during sedimentary processes from source to deposition (Winchester and Floyd, 1977; Zheng et al., 2020), and they can generally be used as reliable geochemical indicators of sediment provenance (Yang et al., 2022). Pearce (2008) suggested using the Nb/Yb ratio for distinguishing basalts of different origins (subduction-related and within-plate) and ages. In this study, we synthesize Nb/Y vs. Zr/TiO_2, Al_2O_3/TiO_2 vs. Nb/Yb, REE distribution patterns and an upper continental crust normalized trace element spider to determine sediment provenances.

As shown in Fig. 4, the Nb/Y vs. Zr/TiO_2 and Al_2O_3/TiO_2 vs. Nb/Yb diagrams indicate that most samples overlap with or are close to the high-Ti basalts of the Emeishan LIP, and are distinctly separated from low-Ti basalts. Sample X-2 taken from near the top of Xuanwei Formation is close to the Permian/Triassic volcanic ash and andesite region of the diagram, and this sample probably contains felsic volcanic ash components of mixed origin. These results are consistent with previous studies in which volcanic ashes in the topmost coal in the Xuanwei Formation are seen to derive from the felsic magmatic arc (He et al., 2014; Wang et al., 2018). Most samples show similar geochemical characteristics to the high-Ti basalts (Fig. 4A, B). These sediment provenances are further corroborated by the Upper Continental Crust (UCC)-normalized trace element spider (Fig. 4C). The chondrite-normalized REE patterns of most samples have low Eu anomalies and are enriched in light REEs, again similar to high-Ti basalts (Fig. 4D). Thus, various geochemical parameters indicate that sediment was sourced from Emeishan LIP high-Ti basalts throughout the Permian-Triassic boundary interval in southwestern China.

Basalt weathering is sensitive to climatic conditions (Li et al., 2016; Chen et al., 2020) and has been advocated as a major driver of climate change in the tropical humid belt in Earth's deep past (Yang et al., 2022). In latest Permian and earliest Triassic times, the South China block was located near the equator (Huang et al., 2018) and experienced humid and warm climatic conditions and rapidly increasing temperatures (Chen et al., 2016). Changing CIA values generally reflect chemical weathering trends of source rock (Xu and Shao, 2018). Yang et al. (2022) evaluated the influence of chemical weathering on basaltic source material from the Emeishan LIP and suggested that changes in the CIA of mudstone samples reflect chemical weathering in basaltic landscapes. Our results denote a slight decrease in weathering intensity at the top of the Xuanwei Formation, followed by strong weathering in the Kayitou Formation. Subsequently, a distinct and rapid decrease in weathering intensity occurred during deposition of the top of the Kayitou Formation and the lower part of the Dongchuan Formation (Fig. 2). The anomalous decrease in basaltic weathering intensity in the earliest Triassic is similar to patterns observed in the northern Youjiang Basin (Yang et al., 2022). This anomaly has potential origins in the acceleration of physical erosion. In the modern landscape, strong physical erosion is considered to be related to the consequences of exposure of bare soils following large-scale deforestation (Ruprecht and Schofield, 1991; Yan et al., 2019). This assumption is consistent with global-scale plant extinctions during the PTME (Benton and Newell, 2014). We further calculated the denudation rate from the geochemical data in order to determine the horizon at which increased erosion of the basalt landscape began (Yang et al., 2022; see Supplementary Materials for the detailed methods used for this analysis). The calculated denudation rate for the basalt landscape in the Xuanwei Formation is low ($\sim$140 $t/km^2/yr$) but this rate increases at the top of the Xuanwei Formation ($\sim$280 $t/km^2/yr$), slightly earlier than the onset of CIE-1 (Fig. 2). The denudation rate remained high through deposition of the Kayitou Formation before accelerating further in its upper part

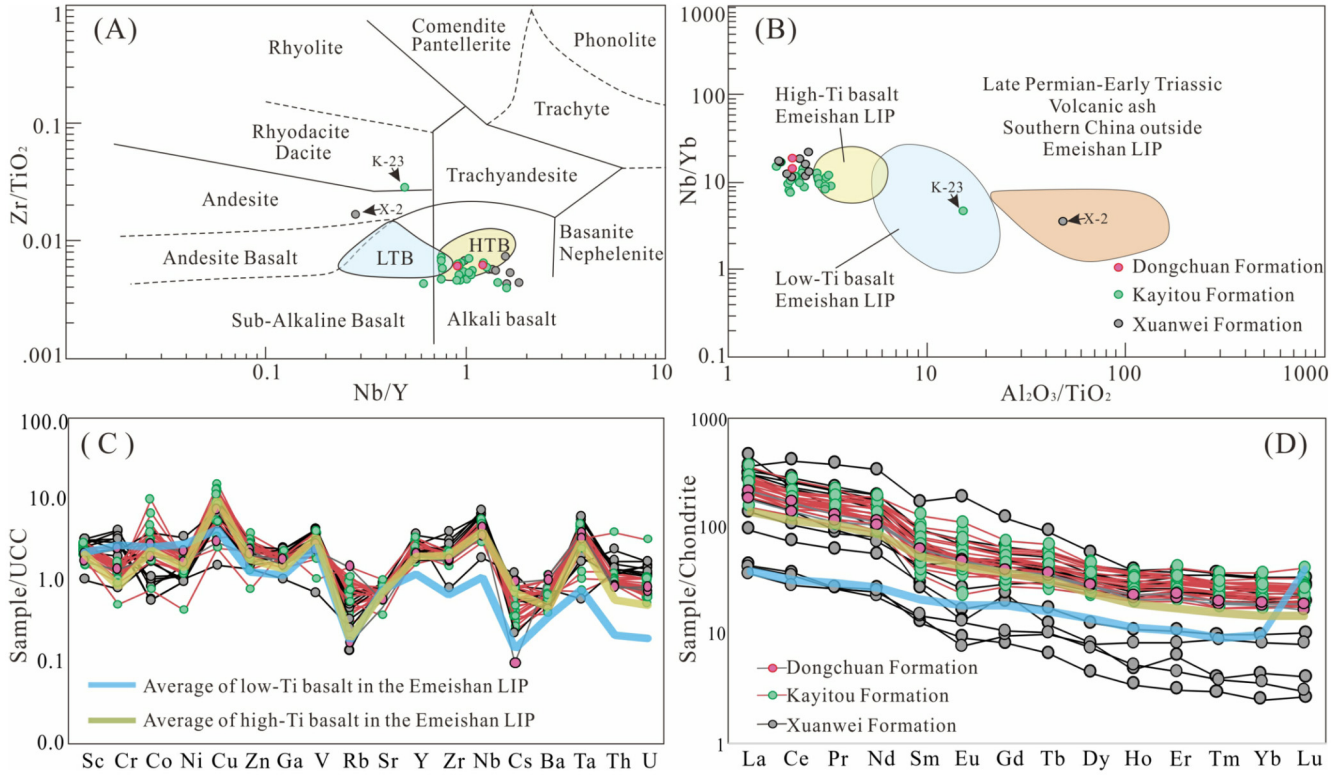

Fig. 4. Geochemical plots of Nb/Y vs. Zr/TiO_2 from Winchester and Floyd (1977) and Al_2O_3/TiO_2 vs. Nb/Yb from Zheng et al. (2020). Upper continental crust (Taylor et al., 1981) normalized trace element spider. Chondrite (Sun and McDonough, 1989) normalized rare earth element patterns.

and into the Dongchuan Formation, when denudation was ~ 5–10 times faster than the pre-extinction baseline (Fig. 2). Our results are consistent with estimates of the erosion rate in Youjiang Basin of South China that shows two rapid acceleration events, firstly at the end of the Permian and then again in the earliest Triassic (Yang et al., 2022).

5.2. The timeframe for the Permian-Triassic boundary

Earlier studies placed the terrestrial PTB near the base of the Dongchuan Formation (Shen et al., 2011; Zhang et al., 2016). However, plant megafossils and palynomorphs indicate that *Gigantopteris* peat-forming ecosystems collapsed at the base of the Kayitou Formation (Yu et al., 2015; Feng et al., 2020; Xu et al., 2022). Zircon U–Pb dates (250.3±2.1 Ma and 252.0±2.1 Ma) and carbon isotope values for the uppermost coal in the Xuanwei Formation (C1) suggest that the PTB lies within this bed (Wang et al., 2018). However, more recent high-precision dating using CA-ID-TIMS (251.93±0.096 Ma and 252.29±0.03 Ma; Wu, 2020) supports placement of the PTB just above the C1 coal (Fig. 3). Unfortunately, the discontinuous distribution of the C1 coal has resulted in a lack of consensus on the placement of the PTB in terrestrial strata (Shen et al., 2011; Zhang et al., 2016, 2021).

A well-known latest Permian large, negative carbon isotope excursion and contemporaneous peaks in sedimentary Hg concentration have been attributed to the emplacement of the Siberian Traps LIP during the PTME (Dal Corso et al., 2022) and the PTB is usually placed just above these phenomena in marine successions (Chu et al., 2020). A similar negative $\delta^{13}C_{org}$ excursion and Hg anomaly are seen in the strata just above the C1 coal in borehole H401, providing an independent chemostratigraphic tool for the placement of the PTB. We suggest that CIE-1 and the contemporary Hg/TOC peak in borehole H401 (Fig. 2) corresponds to the latest Permian CIE and Hg peak in marine strata at the Meishan PTB Global Stratotype Section and Point (GSSP; Fig. 5). Anchoring the floating astronomical timescale to radioisotopic ages from Meishan facilitates the establishment of a temporal framework for our borehole successions based on absolute age dates and our spectral gamma-ray analysis (Fig. 5). When the PTB (251.902 ±0.024 Ma) is anchored, cycle-tuned ages in borehole H401 fit radio-isotope dates of ash beds in C1 (Fig. 5). Li et al. (2016) identified three 405 kyr cycles in the Permian–Triassic transition based on GR data from Meishan. The interval comprising these three cycles can be correlated between the H401 borehole record and Meishan (Fig. 5), further demonstrating the reliability of our results. Xie et al. (2007) found that carbonate carbon isotopes exhibit two gradual, but major shifts across the PTB at Meishan and these are reproducible in other Tethys Ocean records. These two CIEs can be correlated between H401 and Meishan, facilitating estimation of the overall duration of carbon cycle destabilization (CIE-1 onset to CIE-2 conclusion) in our core successions. We estimate this destabilization to have lasted 0.6 ± 0.1 Myr (1.5 x long eccentricity cycles or 6.5 x eccentricities; Fig. 5). This estimate is slightly longer than the duration (427 kyr ± 79 kyr) of carbonate carbon isotope disturbances at Meishan proposed by Burgess et al. (2014) but the Meishan record is highly condensed, perhaps masking the true astrochronology of that setting (Song et al., 2013; S.Z. Shen et al., 2019). Our data is, however, consistent with the 600–700 kyr cyclostratigraphic estimate of the duration of the PTB turnover at Shangsi in Sichuan (Huang et al., 2011).

5.3. A protracted, two-step terrestrial extinction

The main marine extinction in South China spans the *Clarkina meishanensis* and *Isarcicella isarcica* conodont biozones, and while statistical analyses of fossil data support a single, brief catastrophic event (S.Z. Shen et al., 2011, 2019; Burgess et al., 2014), some have identified two extinction pulses near the PTB (Xie et al., 2007; Song et al., 2013; Su et al., 2021). In addition, increasing evidence showed the terrestrial crisis likely occurred in two stages in SW

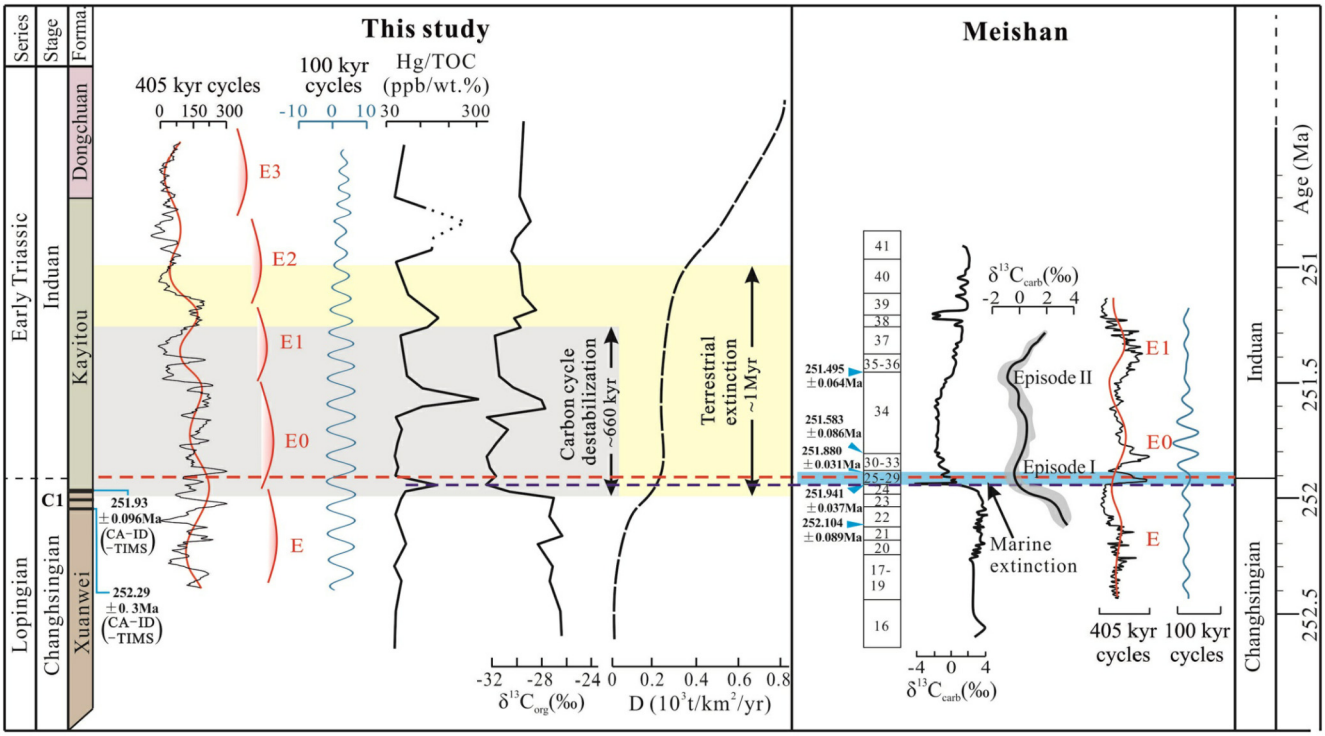

Fig. 5. Astronomical cycle correlations between the marine Permian-Triassic global stratotype section at Meishan and the terrestrial records studied here. The timeframe is based on filtered 100 kyr (e) and 405 kyr (E) eccentricity cycles in the H401 core. Age data for Meishan are from Burgess et al. (2014). $\delta^{13}C_{carb}$ data for Meishan are from Burgess et al. (2014; left panel) and Xie et al. (2007; middle panel) and the astronomical cycles are from Li et al. (2016; right panel). Age data for the study area are from Wang et al. (2018) and Wu (2020). Red dashed lines = PTB. Blue dashed lines = Carbon isotope and Hg/TOC correlations between Meishan and the H401 core. Abbreviation: Forma. = Formation.

China (Aftabuzzaman et al., 2021; Huang et al., 2022). Our data suggest a period of intense weathering during deposition of the Kayitou Formation was followed by a rapid decline in chemical weathering intensity at the top of the Formation that persisted into the Dongchuan Formation (Fig. 2). The decrease in basaltic chemical weathering in the earliest Triassic might be related to accelerated physical erosion (Yang et al., 2022), a consequence of large-scale deforestation and exposure of bare soils (Ruprecht and Schofield, 1991; Yan et al., 2019). The denudation rate of the basaltic landscape increased at the top of Xuanwei Formation and again in the upper Kayitou Formation, levels that are ~1 Myr apart based on our astronomical timescale (Fig. 5). This suggested time span for terrestrial disturbances is consistent with duration on the extinction interval based on the tetrapod fossil record of locations as distant as South Africa (Viglietti et al., 2021).

Late Permian tropical *Gigantopteris* rainforests were the main source of coal in SW China and provided habitat for terrestrial animals (Yu et al., 2015). The disappearance of these forests dramatically disrupted non-marine ecosystems (Shao et al., 2020). Previous studies of plant macrofossils indicated the replacement of stable pteridophyte-dominated floras by rapidly growing communities dominated by lycopods at the base of the Kayitou Formation (Feng et al., 2020; Xu et al., 2022). Plant diversity dropped as pteridophyte-dominated floras collapsed during the first pulse of the PTME at the base of the Kayitou Formation (Yu et al., 2015; Feng et al., 2020). Volcanism, along with enhanced wildfire, may have contributed to plant crisis at this level (Shen et al., 2011; Lu et al., 2022). However, plants are autotrophic primary producers and are not particularly susceptible to abrupt extinction (Benton and Newell, 2014), and moderately rich conifer and pteridosperm-dominated floras were soon established (Yu et al., 2015; Xiong and Wang, 2016; Xu et al., 2022). Although devastating, the first extinction pulse did not lead to the total collapse of terrestrial ecosystems in SW China. Increasing evidence suggests that the final deforestation event occurred not at the end of the Permian, but during the Induan (Schneebeli-Hermann et al., 2017; Liu et al., 2020). Increased aridity and widespread wildfires in the earliest Triassic were likely lethal factors in the terrestrial extinction scenario (Yan et al., 2019; Chu et al., 2020; Cai et al., 2021).

Sedimentary Hg is a powerful proxy for volcanism (Grasby et al., 2019). Hg concentration peaks are known from both marine and terrestrial PTB successions in South China (Shen et al., 2011; J. Shen et al., 2019), where they appear to coincide with the onset of extinctions (Grasby et al., 2019). The onset of CIE-1 and the contemporary Hg/TOC peak in our data (Fig. 5) suggests a relationship between volcanism and the first terrestrial extinction pulse. In contrast, CIE-2 has no accompanying Hg/TOC peak, suggesting that volcanism did not drive the second extinction pulse, but perhaps instead was responsible for the delayed recovery in terrestrial ecosystems (Retallack et al., 2011). Increased aridity and wildfires in the earliest Triassic may have contributed to losses (Yan et al., 2019; Cai et al., 2021). Regional, felsic volcanism in South China potentially had further deleterious environmental effects during this interval (Zhang et al., 2021). We suggest that the second, more drastic denudation rate increase, accompanied by high rates of physical erosion in the Early Triassic (upper Kayitou Formation), marks the complete collapse of terrestrial plant ecosystems and the culmination of the terrestrial PTME. The full duration of the terrestrial PTME is estimated to be ~1 Myr, in stark contrast with the much more abrupt marine PTME that was probably over within as little as a few tens of thousands of years (Burgess et al., 2014; S.Z. Shen et al., 2019). This long duration of the terrestrial crisis has implications for extinction scenarios in which terrestrial losses drove the marine crisis through increased runoff, eutrophication and anoxia (Benton and Newell, 2014; Yan et al., 2019; Huang et al., 2022; see also Dal Corso et al., 2022 for a review) because the relationship between losses on land and in the oceans is more complex than previously thought and full deforestation in

SW China did not take place until after the conclusion of the marine extinction crisis.

6. Conclusion

A combined chemostratigraphic and astronomical timescale for boreholes cored through the Permian-Triassic boundary interval in southwest China provides a framework for evaluating the timing and causes of the Permian-Triassic terrestrial extinction. Two negative carbon isotope excursions (CIEs) occur between the top of the Xuanwei Formation and the middle of the Kayitou Formation. Cyclostratigraphy indicates that these two CIEs occurred within a period of carbon cycle destabilization lasting 0.6 ± 0.1 Myr. We calculate the total erosion rates for basaltic landscapes through the late Permian to earliest Triassic interval and these reveal two phases of increased denudation rates. The first increase in denudation of the land surface was synchronous with the onset of the first negative carbon isotope excursion and it led to a ∼1.5–2 times increase in erosion rate. This level likely correlates with the initial wave of terrestrial plant losses at the end of the Permian. The second, more significant increase in denudation rate saw erosion rates rise to ∼5–10 times pre-extinction levels and this represents the final collapse of terrestrial plant systems. This full duration of terrestrial ecosystem disturbance is estimated to be ∼1 Myr. Taken together, the negative $\delta^{13}C$ excursions and sedimentary Hg anomalies within our astrochronological framework suggest that the onset of terrestrial extinction losses in SW China occurred prior to the marine PTME, but crisis on land concluded much later than in the oceans. It is becoming increasingly evident that globally, the terrestrial PTME was diachronous. Whether these differing patterns of extinction are rooted in differences in latitude, biodiversity and ecological stress is highly relevant to the modern phase of global change, but this is yet be evaluated.

CRediT authorship contribution statement

Fanghui Hua: Conceptualization, Data curation, Formal analysis, Investigation, Methodology, Software, Supervision, Visualization, Writing – original draft, Writing – review & editing. **Longyi Shao:** Conceptualization, Funding acquisition, Supervision, Writing – review & editing. **Tianchang Zhang:** Methodology. **David P.G. Bond:** Supervision, Validation, Writing – review & editing. **Xuetian Wang:** Investigation, Methodology, Software. **Juan Wang:** Methodology. **Zhiming Yan:** Investigation, Methodology. **Jing Lu:** Writing – review & editing. **Jason Hilton:** Funding acquisition, Supervision, Validation, Writing – review & editing.

Declaration of competing interest

The authors declare that they have no known competing financial interests or personal relationships that could have appeared to influence the work reported in this paper.

Data availability

Data will be made available on request.

Acknowledgements

This study was supported by the National Natural Science Foundation of China (41572090), Fundamental Research Funds for Central Universities (2022YJSDC05), Yueqi Scholar Fund of China University of Mining and Technology (Beijing) and the Natural Environment Research Council (NE/P013724/1). We thank Editor Andrew Jacobson plus Christopher Fielding and another anonymous reviewer for their constructive comments.

Appendix A. Supplementary material

Supplementary material related to this article can be found online at https://doi.org/10.1016/j.epsl.2023.118035.

References

Aftabuzzaman, M., Kaiho, K., Biswas, R.K., Liu, Y., Saito, R., Tian, L., Bhat, G.M., Chen, Z.-Q., 2021. End-Permian terrestrial disturbance followed by the complete plant devastation, and the vegetation proto-recovery in the earliest-Triassic recorded in coastal sea sediments. Glob. Planet. Change 205, 103621. https://doi.org/10.1016/j.gloplacha.2021.103621.

Benton, M.J., Newell, A.J., 2014. Impacts of global warming on Permo–Triassic terrestrial ecosystems. Gondwana Res. 25, 1308–1337. https://doi.org/10.1016/j.gr.2012.12.010.

Bercovici, A., Cui, Y., Forel, M.B., Yu, J.X., Vajda, V., 2015. Terrestrial paleoenvironment characterization across the Permian–Triassic boundary in South China. J. Asian Earth Sci. 98, 225–246. https://doi.org/10.1016/j.jseaes.2014.11.016.

Burgess, S.D., Bowring, S.A., Shen, S.Z., 2014. High-precision timeline for Earth's most severe extinction. Proc. Natl. Acad. Sci. 111 (9), 3316–3321. https://doi.org/10.1073/pnas.1317692111.

Cai, Y.F., Zhang, H., Feng, Z., Shen, S.Z., 2021. Intensive wildfire associated with volcanism promoted the vegetation changeover in southwest China during the Permian-Triassic transition. Front. Earth Sci. 9, 615841. https://doi.org/10.3389/fe2021.615841.

Chen, J., Shen, S.Z., Li, X.H., Xu, Y.G., Joachimski, M.M., Bowring, S.A., Erwin, D.H., Yuan, D.X., Chen, B., Zhang, H., Wang, Y., Cao, C.Q., Zheng, Q.F., Mu, L., 2016. High-resolution SIMS oxygen isotope analysis on conodont apatite from South China and implications for the end-Permian mass extinction. Palaeogeogr. Palaeoclimatol. Palaeoecol. 448, 26–38.

Chen, Y., Hedding, D.W., Li, X., Greyling, A.C., Li, G., 2020. Weathering dynamics of Large Igneous Provinces (LIPs): a case study from the Lesotho highlands. Earth Planet. Sci. Lett. 530, 115871. https://doi.org/10.1016/j.epsl.2019.115871.

Chu, D.L., Grasby, S.E., Song, H., Corso, J.D., Wang, Y., Mather, T.A., Wu, Y., Song, H., Shu, W., Tong, J., Wignall, P.B., 2020. Ecological disturbance in tropical peatlands prior to marine Permian-Triassic mass extinction. Geology 48 (3), 288–292.

Cui, Y., Li, M.S., van Soelen, E.E., Peterse, F., Kürschner, W.M., 2021. Massive and rapid predominantly volcanic CO_2 emission during the end-Permian mass extinction. Proc. Natl. Acad. Sci. USA 118, 2014701118. https://doi.org/10.1073/pnas.2014701118.

Dal Corso, J., Song, H.J., Callegaro, S., Chu, D.L., Sun, Y.D., Hilton, J., Grasby, S.E., Joachimski, M.M., Wignall, P.B., 2022. Environmental crises at the Permian–Triassic mass extinction. Nat. Rev. Earth Environ. 3, 197–214.

Erwin, D.H., 2015. Extinction: How Life on Earth Nearly Ended 250 Million Years Ago, updated edition. Princeton University Press.

Fedo, C.M., Nesbitt, H.W., Young, G.M., 1995. Unravelling the effects of potassium metasomatism in sedimentary rocks and paleosols, with implications for paleoweathering conditions and provenance. Geology 23 (10), 921–924.

Feng, Z., Wei, H.B., Guo, Y., He, X.Y., Sui, Q., Zhou, Y., Liu, H.Y., Gou, X.D., Lv, Y., 2020. From rainforest to herbland: new insights into land plant responses to the end-Permian mass extinction. Earth-Sci. Rev. 204, 103153. https://doi.org/10.1016/j.earscirev.2020.103153.

Fielding, C.R., Frank, T.D., McLoughlin, S., Vajda, V., Mays, C., Tevyaw, A.P., Winguth, A., Winguth, C., Nicoll, R.S., Bocking, M., Crowley, J.L., 2019. Age and pattern of the southern high-latitude continental end-Permian extinction constrained by multiproxy analysis. Nat. Commun. https://doi.org/10.1038/s41467-018-07934-z.

Grasby, S.E., Them, T.R., Chen, Z.H., Yin, R.S., Ardakani, O.H., 2019. Mercury as a proxy for volcanic emissions in the geologic record. Earth-Sci. Rev. 196, 102880. https://doi.org/10.1016/j.earscirev.2019.102880.

He, B., Zhong, Y.T., Xu, Y.G., Li, X.H., 2014. Triggers of Permo-Triassic boundary mass extinction in South China: the Siberian traps or paleo-tethys ignimbrite flare-up? Lithos 204, 258–267.

Hinnov, L.A., 2013. Cyclostratigraphy and its revolutionizing applications in the Earth and planetary sciences. Geol. Soc. Am. Bull. 125, 1703–1734. https://doi.org/10.1130/B30934.1.

Huang, B.C., Yan, Y.G., Piper, J.D.A., Zhang, D.H., Yi, Z.Y., Yu, S., Zhou, T.H., 2018. Paleomagnetic constraints on the paleogeography of the East Asian blocks during late Paleozoic and early Mesozoic times. Earth-Sci. Rev. 186, 8–36. https://doi.org/10.1016/j.earscirev.2018.02.004.

Huang, C.J., Tong, J.N., Hinnov, L., Chen, Z.Q., 2011. Did the great dying of life take 700 k.y.? Evidence from global astronomical correlation of the Permian-Triassic boundary interval. Geology 40 (5), e267. https://doi.org/10.1130/G33200Y.1.

Huang, H., Gao, Y., Ma, C., Jones, M.M., Zeeden, C., Ibarra, D.E., Wu, H., Wang, C., 2021. Organic carbon burial is paced by a ∼173-ka obliquity cycle in the middle to high latitudes. Sci. Adv. 7 (28), eabf9489. https://doi.org/10.1126/sciadv.abf9489.

Huang, Y.F., He, W.H., Liao, W., Wang, Y.B., Yi, Z.X., Yang, H., Li, G.S., 2022. Two pulses of increasing terrestrial input to marine environment during the Permian–Triassic transition. Palaeogeogr. Palaeoclimatol. Palaeoecol. 586. https://doi.org/10.1016/j.palaeo.2021.110753.

Li, M.S., Ogg, J., Zhang, Y., Huang, C.J., Hinnov, L., Chen, Z.Q., Zou, Z.Y., 2016. Astronomical tuning of the end-Permian extinction and the early Triassic epoch of South China and Germany. Earth Planet. Sci. Lett. 441, 10–25. https://doi.org/10.1016/j.epsl.2016.02.017.

Li, M.S., Kump, L.R., Hinnov, L.A., Mann, M.E., 2018. Tracking variable sedimentation rates and astronomical forcing in Phanerozoic paleoclimate proxy series with evolutionary correlation coefficients and hypothesis testing. Earth Planet. Sci. Lett. 501, 165–179. https://doi.org/10.1016/j.epsl.2018.08.041.

Li, M.S., Hinnov, L., Kump, L., 2019. Acycle: time-series analysis software for paleoclimate research and education. Comput. Geosci. 127, 12–22. https://doi.org/10.1016/j.cageo.2019.02.011.

Liu, F., Peng, H.P., Bomfleur, B., Kerp, H., Zhu, H.C., Shen, S.Z., 2020. Palynology and vegetation dynamics across the Permian–Triassic boundary in southern Tibet. Earth-Sci. Rev. 209, 103278. https://doi.org/10.1016/j.earscirev.2020.103278.

Lu, J., Wang, Y., Yang, M.F., Zhang, P.X., Bond, D.P.G., Shao, L.Y., Hilton, J., 2022. Diachronous end-Permian terrestrial ecosystem collapse with its origin in wildfires. Palaeogeogr. Palaeoclimatol. Palaeoecol. 594, 110960. https://doi.org/10.1016/j.palaeo.2022.110960.

Ma, C., Meyers, S.R., Sageman, B.B., 2017. Theory of chaotic orbital variations confirmed by Cretaceous geological evidence. Nature 542 (7642), 468–470.

Panahi, A., Young, G.M., Rainbird, R.H., 2000. Behavior of major and trace elements (including REE) during Paleoproterozoic pedogenesis and diagenetic alteration of an Archean granite near Ville Marie, Québec, Canada. Geochim. Cosmochim. Acta 64 (13), 2199–2220.

Pearce, J.A., 2008. Geochemical fingerprinting of oceanic basalts with applications to ophiolite classification and the search for Archean oceanic crust. Lithos 100, 14–48.

Retallack, G.J., Sheldon, N.D., Carr, P.F., Fanning, M., Thompson, C.A., Williams, M.L., Jones, B.G., Hutton, A., 2011. Multiple early Triassic greenhouse crises impeded recovery from late Permian mass extinction. Palaeogeogr. Palaeoclimatol. Palaeoecol. 308, 233–251.

Ruprecht, J.K., Schofield, N.J., 1991. Effects of partial deforestation on hydrology and salinity in high salt storage landscapes. II. Strip, soils and parkland clearing. J. Hydrol. 129, 39–55. https://doi.org/10.1016/0022-1694(91)90043-H.

Schneebeli-Hermann, E., Hochuli, P.A., Bucher, H., 2017. Palynofloral associations before and after the Permian–Triassic mass extinction, Kap Stosch, East Greenland. Glob. Planet. Change 155, 178–195. https://doi.org/10.1016/j.gloplacha.2017.06.009.

Shao, L.Y., Gao, C.X., Zhang, C., Wang, H., Guo, L.J., Gao, C.H., 2013. Sequence-palaeogeography and coal accumulation of late Permian in southwestern China. Acta Sedimentological Sin. 31 (5), 856–866.

Shao, L.Y., Wang, X.T., Wang, D.D., Li, M.P., Wang, S., Li, Y.J., Shao, K., Zhang, C., Gao, C.X., Dong, D.X., Cheng, A.G., Lu, J., Ji, C.W., Gao, D., 2020. Sequence stratigraphy, paleogeography, and coal accumulation regularity of major coal-accumulating periods in China. Int. J. Coal Sci. Technol. 7, 240–262. https://doi.org/10.1007/s40789-020-00341-0.

Shen, J., Yu, J.X., Chen, J.B., Thomas, J.A., Xu, G.Z., Feng, Q.L., Shi, X., Noah, J.P., Shu, W.C., Xie, S.C., 2019. Mercury evidence of intense volcanic effects on land during the Permian-Triassic transition. Geology 47 (12), 1117–1121. https://doi.org/10.1130/G46679.1.

Shen, S.Z., Crowley, J.L., Wang, Y., Bowring, S.A., Erwin, D.H., Sadler, P.M., Cao, C.Q., Rothman, D.H., Henderson, C.M., Ramezani, J., Zhang, H., Shen, Y., Wang, X.D., Wang, W., Mu, L., Li, W.Z., Tang, Y.G., Liu, X.L., Liu, L.J., Zeng, Y., Jiang, Y.F., Jin, Y.G., 2011. Calibrating the end-Permian mass extinction. Science 334, 1367–1372. https://www.science.org/doi/10.1126/science.1213454.

Shen, S.Z., Ramezani, J., Chen, J., Cao, C.Q., Erwine, D.H., Zhang, H., Xiang, L., Erwin, D.H., Henderson, C.M., Zhen, F.Q., Bowring, S.A., Wang, Y., Li, X.H., Wang, X.D., Yuan, D.X., Zhang, Y.C., Mu, L., Wu, Y.S., 2019. A sudden end-Permian mass extinction in South China. Geol. Soc. Am. Bull. 131, 205–223. https://doi.org/10.1130/B31909.1.

Song, H.J., Wignall, P.B., Tong, J.N., Yin, H.F., 2013. Two pulses of extinction during the Permian-Triassic crisis. Nat. Geosci. 6, 52–56. https://doi.org/10.1038/ngeo1649.

Su, C., Chen, Z.Q., Wang, X., Wu, S., Guo, Z., 2021. Biotic and palaeoecological variations in the Permian-Triassic boundary microbialite (Xiejiacao, South China): implication for a two-phase ecological crisis in microbialite ecosystems. Glob. Planet. Change 207, 103679.

Sun, S.S., McDonough, W.F., 1989. Chemical and isotopic systematics of oceanic basalts: implications for mantle composition and processes. Geol. Soc. (Lond.) Spec. Publ. 42 (1), 313–345.

Taylor, S.R., McLennan, S.M., Armstrong, R.L., Tarney, J., 1981. The composition and evolution of the vontinental crust: rare Earth element evidence from sedimentary rocks [and discussion]. Philos. Trans. R. Soc. Lond. Ser. A, Math. Phys. Sci. 301 (1461), 381–399. https://www.jstor.org/stable/37026.

Trümper, S., Gaitzsch, B., Schneider, J.W., Ehling, B.C., Kleeberg, R., Rößler, R., 2020. Late Palaeozoic red beds elucidate fluvial architectures preserving large woody debris in the seasonal tropics of central Pangaea. Sedimentology 67, 1973–2012. https://doi.org/10.1111/sed.12692.

Viglietti, P.A., Benson, R.B.J., Smith, R.M.H., Botha, J., Kammerer, C.F., Skosan, Z., Butler, E., Crean, A., Eloff, B., Kaal, S., Mohoi, J., Molehe, W., Mtalana, N., Mtungata, S., Ntheri, N., Ntsala, T., Nyaphuli, J., October, P., Skinner, G., Strong, M., Stummer, H., Wolvaardt, F.P., Angielczyk, K.D., 2021. Evidence from South Africa for a protracted end-Permian extinction on land. Proc. Natl. Acad. Sci. USA 118 (17), e2017045118. https://doi.org/10.1073/pnas.2017045118.

Wang, J., Shao, L.Y., Wang, H., Spiro, B., Large, D.J., 2018. SHRIMP zircon U-Pb ages from coal beds across the Permian-Triassic boundary, eastern Yunnan, southwestern China. J. Paleogeogr. 7, 117–129. https://doi.org/10.1016/j.jop.2018.01.002.

Wang, X.T., Shao, L.Y., Eriksson, K.A., Yan, Z.M., Wang, J.M., Li, H., Zhou, R.X., Lu, J., 2020. Evolution of a plume-influenced source-to-sink system: an example from the coupled central Emeishan large igneous province and adjacent western Yangtze cratonic basin in the late Permian, SW China. Earth-Sci. Rev. 207, 103224. https://doi.org/10.1016/j.earscirev.2020.103224.

Wignall, P.B., Chu, D., Hilton, J., Corso, J.D., Wu, Y., Wang, Y., Atkinson, J., Tong, J., 2020. Death in the shallows: the record of Permo-Triassic mass extinction in paralic settings, southwest China. Glob. Planet. Change 189, 103176. https://doi.org/10.1016/j.gloplacha.2020.103176.

Winchester, J.A., Floyd, P.A., 1977. Geochemical discrimination of different magma series and their differentiation products using immobile elements. Chem. Geol. 20, 325–343.

Wu, H.C., Zhang, S.H., Hinnov, L.A., Jiang, G.Q., Feng, Q.L., Li, H.Y., Yang, T.S., 2013. Time-calibrated Milankovitch cycles for the late Permian. Nat. Commun. 4, 2452. https://doi.org/10.1038/ncomms3452.

Wu, Q., 2020. High-precision zircon U-Pb geochronological studies of the Permian ash beds from China and North America. PhD. University of Science and Technology of China (in Chinese with English abstract).

Xiao, L., Xu, Y.G., Mei, H.J., Zheng, Y.F., He, B., Pirajno, F., 2004. Distinct mantle sources of low-Ti and high-Ti basalts from the western Emeishan large igneous province, SW China: implications for plume–lithosphere interaction. Earth Planet. Sci. Lett. 228 (3–4), 525–546.

Xie, S.C., Pancost, R.D., Huang, J.H., Wignall, P.B., Yu, J.X., Tang, X.Y., Chen, L., Huang, X.Y., Lai, X.L., 2007. Changes in the global carbon cycle occurred as two episodes during the Permian–Triassic crisis. Geology 35 (12), 1083–1086.

Xiong, C.H., Wang, Q., 2016. Permian–Triassic land-plant diversity in South China: was there a mass extinction at the Permian/Triassic boundary? Paleobiology 37 (1), 157–167.

Xu, X.T., Shao, L.Y., 2018. Limiting factors in utilization of chemical index of alteration of mudstones to quantify the degree of weathering in provenance. J. Palaeogeogr. 20 (3), 515–522 (in Chinese with English abstract).

Xu, Y.C., Jiang, R., Deng, Y.Z., Kemp, D.B., Yang, Z.Y., Huang, Ch.J., Zhu, Z.M., 2020. A robust geochronology of the Yangtze River Delta based on magnetostratigraphy and cyclostratigraphy of sediment core ZKA2. Palaeogeogr. Palaeoclimatol. Palaeoecol. 541, 109532. https://doi.org/10.1016/j.palaeo.2019.109532.

Xu, Z., Hilton, J., Yu, J.X., Wignall, P.B., Yin, H.F., Xue, Q., Ran, W.J., Hui, L., Shen, J., Meng, F.S., 2022. Mid-Permian to late Triassic plant species richness and abundance patterns in South China: co-evolution of plants and the environment through the Permian-Triassic transition. Earth-Sci. Rev. 232, 104136. https://doi.org/10.1016/j.earscirev.2022.104136.

Yan, Z.M., Shao, L.Y., Glasspool, I.J., Wang, X.T., Wang, H., 2019. Frequent and intense fires in the final coals of the Paleozoic indicate elevated atmospheric oxygen levels at the onset of the end-Permian mass extinction event. Int. J. Coal Geol. 207, 75–83. https://doi.org/10.1016/j.coal.2019.03.016.

Yang, J.H., Cawood, P.A., Condon, D.J., Liu, J.Z., Deng, X.S., Wang, J.F., Du, Y.S., Yuan, D.X., 2022. Anomalous weathering trends indicate accelerated erosion of tropical basaltic landscapes during the Permo-Triassic warming. Earth Planet. Sci. Lett. 577, 117256. https://doi.org/10.1016/j.epsl.2021.117256.

Yu, J.X., Broutin, J., Chen, Z.Q., Shi, X., Li, H., Chu, D.L., Huang, Q.S., 2015. Vegetation changeover across the Permian–Triassic boundary in southwest China: extinction, survival, recovery and palaeoclimate: a critical review. Earth-Sci. Rev. 149, 203–224. https://doi.org/10.1016/j.earscirev.2015.04.005.

Zhang, H., Cao, C.Q., Liu, X.L., Mu, L., Zheng, Q.F., Liu, F., Xiang, L., Liu, L.J., Shen, S.Z., 2016. The terrestrial end-Permian mass extinction in South China. Palaeogeogr. Palaeoclimatol. Palaeoecol. 448, 108–124. https://doi.org/10.1016/j.palaeo.2015.07.002.

Zhang, H., Zhang, F.F., Chen, J.B., Erwin, D.H., Syverson, D.D., Ni, P., Rampino, M., Chi, Z., Cai, Y.F., Xiang, L., Li, W.Q., Liu, S.G., Wang, R.C., Wang, X.D., Feng, Z., Li, H.M., Zhang, T., Cai, H.M., Zheng, W., Cui, Y., Zhu, X.K., Hou, Z.Q., Wu, F.Y., Xu, Y.G., Planavsky, N., Shen, S.Z., 2021. Felsic volcanism as a factor driving the end-Permian mass extinction. Sci. Adv. 7. https://doi.org/10.1126/sciadv.abf8142.

Zheng, X., Dai, S.F., Nechaev, V., Sun, R.Y., 2020. Environmental perturbations during the latest Permian: evidence from organic carbon and Mercury isotopes of a coal-bearing section in Yunnan Province, southwestern China. Chem. Geol. 549, 119680. https://doi.org/10.1016/j.chemgeo.2020.119680.